IJMSD International Journal of Mechanical System Dynamics WILEY

Virtual vibration test rig for fatigue analysis of dozer push arms

Lei Hou[1,2] ⓘ | Weibin Li[3] | Wenyan Gu[1] | Zizheng Sun[4] | Xiangqian Zhu[1,2] |
Jin-Hwan Choi[5]

[1]Key Laboratory of High-Efficiency and Clean Mechanical Manufacture of MOE, National Demonstration Center for Experimental Mechanical Engineering, School of Mechanical Engineering, Shandong University, Jinan, China

[2]Rizhao Research Institute of Shandong University, Rizhao, China

[3]School of Aerospace Engineering, Xiamen University, Xiamen, China

[4]School of Qilu Transportation, Shandong University, Jinan, China

[5]Department of Mechanical Engineering, Kyunghee University, Seoul, South Korea

Correspondence
Xiangqian Zhu, School of Mechanical Engineering, Shandong University, Jinan 250061, China.
Email: xqzhu@sdu.edu.cn

Abstract

To obtain accurate fatigue life results for construction machinery components, acquiring load spectra is crucial, as their authenticity and validity directly determine the precision of the analysis. In working conditions, component attitudes change continuously, but they remain static on the vibration test rig (VTR), so the acquired target signals should match with the actual component attitudes in the driving signal generation. This paper proposes an efficient and economical simulation-based virtual VTR for fatigue analysis of dozers. First, the relationship between the push arm rotation angle and the cylinder stroke is established, since the cylinder strokes can be measured easily in data acquisition experiments. Second, load decomposition is used to determine the attitude relationship between virtual VTR conditions and actual conditions, and target signals are calculated based on this attitude relationship and measured data. According to the system's frequency response function, the driving signals are iterated until the system's response signals converge with the target signals. Finally, the iteratively obtained load spectra are utilized for fatigue life analysis. The results show that the virtual VTR can effectively and accurately obtain the results of fatigue analysis and has engineering application significance.

KEYWORDS
virtual vibration test rig, driving signal generation, component attitudes, fatigue analysis, dozer push arm

1 | INTRODUCTION

The utilization of construction machinery is pervasive across diverse sectors including construction, road development, mining, agriculture, forestry, and national defense projects.[1,2] Owing to the rigorous and continuous loading cycles, the working components are exposed to a complex interplay of various forces, including tensile pressure, bending, torsion, vibration, and impact over extended periods.[3] This prolonged exposure makes these working components susceptible to fatigue damage. Consequently, a thorough assessment of the fatigue life of these working components holds paramount significance for enhancing the reliability in product design.

The fatigue analysis of construction machinery typically involves the utilization of a vibration test rig (VTR).[4–7] The fundamental

principle behind this equipment is to acquire the driving/input signals that closely mirror actual load conditions. In many instances, the random load spectrum is directly input; conducting random fatigue tests necessitates a loading system with high dynamic characteristics. Furthermore, the direct measurement of external loads acting on the structure faces challenges due to environmental influences. Unfortunately, the data obtained from sensors on components during testing represent response signals and cannot be used as the input signals of VTR.[8] Consequently, some researchers have resorted to traditional empirical formulas to estimate working loads. This involves replacing variable soil loads with theoretically calculated constant forces. Yin et al.[9] performed calculations of axial tension and bending moments by leveraging measured cross-section strain. They established a mechanical balance equation to determine the load at each joint of the working components. Bae et al.[10] introduced a technology rooted in engineering data analysis. This technology can extract fatigue design loads from the stress-time history measured by sensors placed in the boom. However, this method is laborious and the results are not precise.

The virtual iteration technique is a method for inversely solving nonlinear systems by simplifying them into linear systems. To mitigate the impact of nonlinear systems on reproducing target signals, it iteratively derives drive signals, enabling the simulation and validation of real system behavior. Virtual iteration is a mathematical operation involving repeated calculations and adjustments to progressively approach the desired solution. White noise is used in a multibody dynamic system to obtain response signals such as displacement, force, and acceleration. These responses are then used to derive the system's frequency response function (FRF). By utilizing the system's inverse FRF, the input is calculated from the output. The iterative process involves comparison of simulated response signals with measured target signals, correcting the error signal by multiplying it with an iteration gain. This process is repeated until the results meet the required iterative accuracy, ultimately outputting the final drive signal. Currently, this method is widely used for high-precision automotive road spectrum acquisition and integrated with component fatigue life simulation analysis. It holds significant engineering value in shortening vehicle development cycles and enhancing vehicle fatigue durability.[11] Oppermann et al.[12] introduced a virtual model of the test rig, encompassing the tested system, surrounding components, boundary conditions, constraints, and actuator forces. Kim and Yim[13] established a multi-body dynamic (MBD) model of a bus based on the rigid–flexible coupling principle, deriving the stress load spectrum through virtual iterative simulation. Another study by Sendur et al.[14] systematically outlined the design of an experimental device to replicate the dynamic and vibration characteristics of a vehicle on a MAST platform. Key performance indicators such as the system mode and FRF were selected for comparing the dynamics of the tested system in the design of a complete vehicle and the rig. Li et al.[15] utilized seat shift and acceleration signals from the cab as expected signals, obtaining the front suspension load spectrum using the virtual iteration technique. They established a seven-axis road simulation test bench for durability verification. Wang et al.[16] decomposed the load using a virtual quasi-

iterative technique and a MBD model. Post-iteration, the simulation signal closely aligned with the test value, enabling fatigue life prediction. Bian et al.[17] obtained the excitation load spectrum applied to the frame through the virtual iteration technique based on data measured in road tests and the established frame-cab MBD model. To expeditiously and effectively validate the fatigue durability of leaf-spring rubber bushings, Ge et al.[18] used six-component wheel center forces obtained from field tests as inputs. Leveraging the rear suspension multibody model as the foundation, the dynamic load of bushing has been extracted. Daley et al.[19] proposed an alternative iteration method derived through an optimization process, achieving required accuracy with significantly fewer iterations, thereby expediting the testing and debugging process. Wang et al.[20] introduced a QNILC algorithm with optimal iterative gain to enhance the convergence speed of the iterative process for automobile durability tests. Muller and Endisch[21] proposed three distinct models for describing system dynamics, testing and comparing them in terms of convergence speed and control accuracy. Most of the existing research on iteration primarily focuses on multi-axle road durability test rigs. Generally, the wheels show minimal oscillation relative to the body, and the suspension may experience only slight oscillations in the context of car testing. The alignment of the vehicle on the road closely mirrors its behavior on the test rigs, so it is easy to identify the displacement of the shock absorber, vertical acceleration, and vertical force at the wheel center as iterative response signals. However, the component attitude relationship of construction machinery significantly differs from that on VTR.[22] Replicating the actual load spectrum is crucial for analyzing the fatigue characteristics of construction machinery components through vibration tests. In addition, the actual working material is distributed over the entire surface of the construction machinery's working components, presenting a complex transfer path.[23] The contact area between the actuator and the working components is small, posing challenges in determining the actuator layout scheme and the model boundary condition setting. Therefore, the design of dynamic characterization of VTR for construction machinery remains largely unexplored.

To overcome these limitations, this paper proposes an efficient and economical simulation-based virtual VTR for fatigue analysis of dozers. Original data, including strain, oil pressure, and cylinder stroke during dozer operation, are acquired through simulations or experiments. The input signals, equivalent to the actual operating load spectrum, are determined using the virtual iteration technique. This signal can be applied to physical or virtual VTR for fatigue analysis, as illustrated in Figure 1.[24] This virtual VTR aims to replace the traditional analysis method based on physical VTR, addressing challenges such as prolonged test cycles, high costs, low efficiency, and the absence of a visual representation of the fatigue life contour.

The remainder of this paper is organized as shown in Figure 2. A brief description of the co-simulation model is presented in Section 2.[25,26] The attitude relative angle relationship between virtual VTR conditions and actual conditions is established in Section 3. The input signals for the actuators are precisely obtained using the
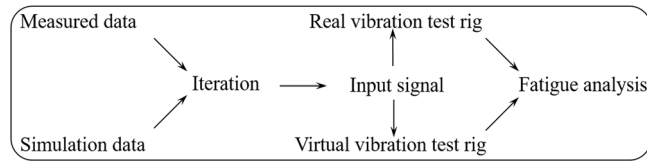
FIGURE 1 Flowchart of accelerated durability analysis using virtual VTR.
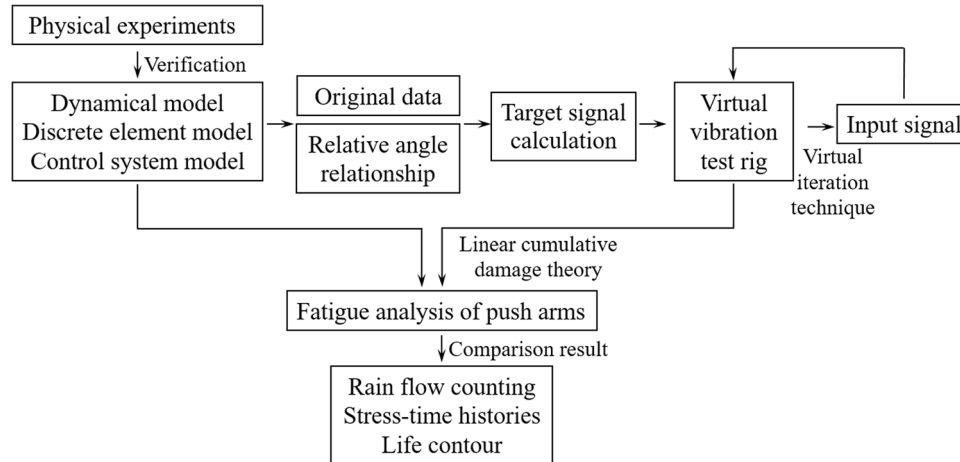

FIGURE 2 Overall concept of this paper.

virtual iteration technique in Section 4. The fatigue analysis results of virtual VTR and co-simulation are presented in Section 5. Finally, concluding remarks are presented in Section 6.

2 | MODEL DEVELOPMENT AND VERIFICATION

To facilitate an intuitive assessment of the results from virtual VTR, we obtained the push arm's time history with the help of high-fidelity simulation, visualized the fatigue life, and used the results to verify the fatigue life results obtained by virtual VTR. This approach allows for a broader perspective and enhances the reliability of our research. Previous studies have successfully modeled straight bulldozing conditions using a RecurDyn–EDEM–AMESim co-simulation[27]; the software is well known in the fields of MBD, DEM, and hydraulic control, respectively. The modeling parameters were meticulously calibrated through physical tests. This method has good potential to acquire load data in situations where it is difficult to conduct physical experiments. As such, we provide a brief explanation of the model development process.

2.1 | Finite element model of working components

The working equipment of the dozer comprises the blade, lift cylinder, tilt cylinder, push arm, pitch arm, and brace, as illustrated in
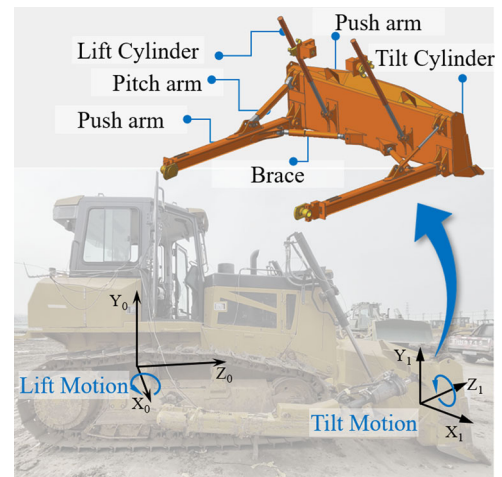

FIGURE 3 Working components of the dozer.

Figure 3. Given that the spherical joint only constrains the relative translational movement between two parts while allowing for relative rotation, the majority of working components are interconnected through spherical joints. This mechanism shows two distinct forms of motion, enabling both the under shovel and lift shovel movements. To analyze the fatigue of the push arm, the modal method is used to transform it into a flexible body.[26,28] Multipoint constraints (MPCs) are utilized to transfer the joint forces acting on the joint markers to the flexible body. In doing so, MPCs introduce artificial stiffness into

the structure, thereby reducing internal stress across the entire area surrounding the contact surface.

2.2 | Discrete element model

Ensuring an accurate soil model is imperative for simulating real external loads.[29] Therefore, a cohesive soil model was meticulously established using EDEM software.[30,31] To control the number of particles, enhance the calculation speed, and maintain consistency with real mechanical properties, the soil model particles were categorized into three parts: bottom, middle, and top particles. The top particles were represented as single spheres with a diameter of 30 mm, while a cluster sphere composed of three spheres was used to model the middle and bottom layers of soil particles, with respective particle sizes of 53 and 66 mm. All three layers of particles adhered to a normal distribution, with a mean value of 1 and a standard deviation of 0.05. Intrinsic parameters, contact parameters, and surface energy for the soil were initially set based on the soil properties of the dozer test site and parameters calibrated in the literature,[32] as detailed in Table 1. The established soil model is depicted in Figure 4, with dimensions of 30 m length, 4.6 m width, and 0.8 m height. Ultimately, the model consisted of 1.29 million soil particles.
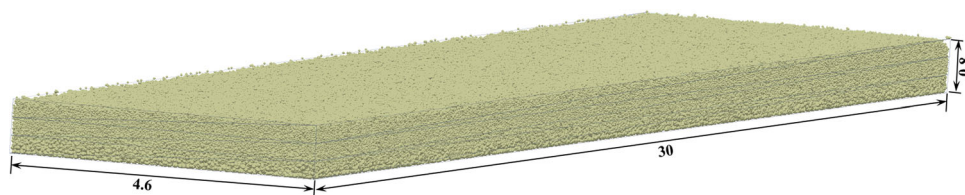
2.3 | Co-simulation

For the co-simulation, RecurDyn facilitates bidirectional data transfer with AMESim and EDEM, as illustrated in Figure 5. RecurDyn conveys the motion information of the tracks and blade to the EDEM geometry at each time step. The motion of the track and blade induces changes in the position of the particles. Simultaneously, EDEM calculates the forces and torques acting on the tracks and blade, forwarding this information to RecurDyn. Meanwhile, RecurDyn utilizes the functional mock-up interface to transmit information about the motion of the sprockets and cylinders to the hydraulic system.[33] In response to the feedback information, the hydraulic system adjusts the required driving torque and oil pressure signal of the hydraulic cylinder using a state chart and PI control, and then transmits this information back to the multibody system. In the subsequent time step, RecurDyn recalculates new displacement and velocity information based on the updated load information and driving force.

2.4 | Physical experiment

Due to the limited sample points collected from current physical experiments, the data are insufficient to determine the push arm's
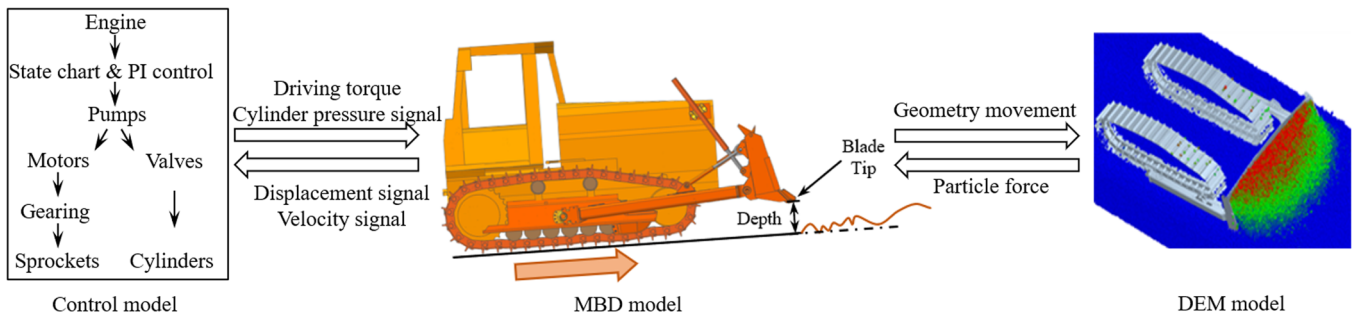
TABLE 1 Parameters of the soil model.

DEM input parameter	Value	DEM input parameter	Value
Soil material properties		Tool (steel) properties	
Density (kg/m³)	2936	Density (kg/m³)	7850
Poisson's ratio	0.3	Poisson's ratio	0.28
Shear modulus (Pa)	2.0×10^7	Shear modulus (Pa)	7.9×10^{10}
Soil–soil interaction		Soil–tool (steel) interaction	
Coefficient of restitution	0.21	Coefficient of restitution	0.32
Coefficient of static friction	0.70	Coefficient of static friction	0.66
Coefficient of rolling friction	0.39	Coefficient of rolling friction	0.21
Hertz–Mindlin with JKR			
Surface energy (J/m²)	10		

FIGURE 4 Soil bed.

FIGURE 5 Data transmission in co-simulation.

FIGURE 6 Physical experiments.

fatigue life and are used only for validating and calibrating the simulation model. According to the findings obtained from the simulation results,[27] the strain of the push arms and oil pressure and strokes of the lift cylinders were measured in the physical experiments illustrated in Figure 6. The axial forces of the push arm were calculated according to the axial strains, material properties, and section area of the push arm, and the driving force of the lift cylinders was calculated according to the oil pressure. The experimental results were compared with those obtained from the simulation, as shown in Figure 7. The driving force of the lift cylinder and the axial force of the push arm fluctuate greatly. Although the travel time of the experiment is slightly shorter than that of the simulation, the experimental average force is in good agreement with the simulated average force. On the basis of the high-fidelity co-simulation model, the control logic is changed to verify the virtual VTR indirectly.

3 | TARGET SIGNAL ACQUISITION

As the strain and oil pressure signals are obtained based on the actual component orientations, the target signals for the virtual VTR are determined in accordance with the attitude relationships. This ensures that the generated input signals for the virtual VTR accurately reflect the equivalent working loads.

3.1 | Attitude relationship of working components

The lifting motion diagram of working components is presented in Figure 8, and only shows the mostly common working conditions: straight bulldozing. The strokes of both lift cylinders are consistent. As illustrated in Figures 9 and 10, the stroke of the tilt cylinder remains at zero, ensuring synchronized movements of the left and right lifting
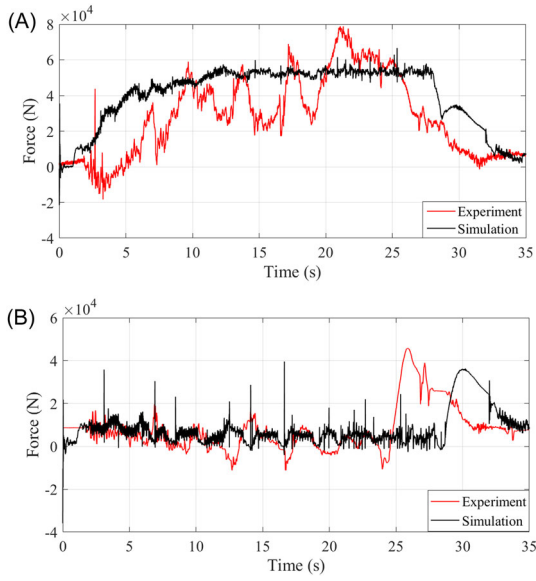
FIGURE 7 Comparison between simulation and physical experiment: (A) axial forces of the push arm and (B) driving forces of the lift cylinder.
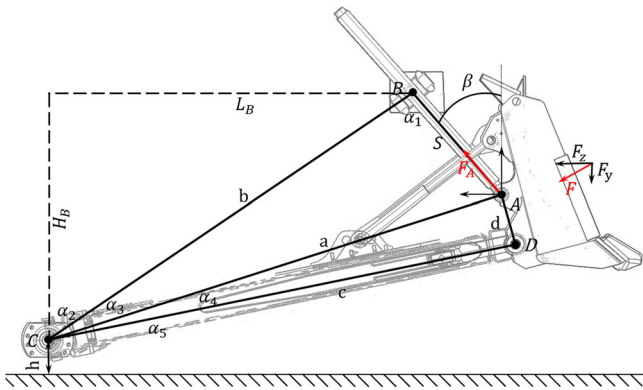

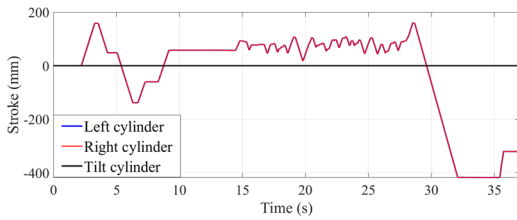**FIGURE 8** Attitude relationship of working components.

FIGURE 9 Cylinder stroke under the straight bulldozing condition.

cylinders in the straight bulldozing condition. The extension and contraction of the lift cylinder facilitate the rotation of the blade and push arm around the joint point on the body. Therefore, the working device moves in a two-dimensional plane, and the established attitude relationship cannot be applied for tilt bulldozing conditions. Throughout this
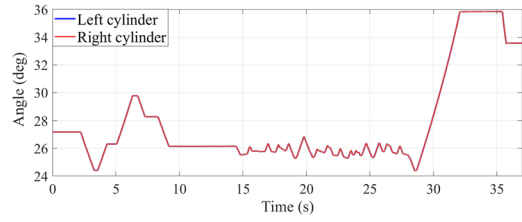

FIGURE 10 Angle between the lift cylinder and the vertical direction.

process, a stable spatial relationship is maintained between the push arm and the blade. The angle β, representing the inclination of the lift cylinder relative to the blade, undergoes real-time changes, resulting in varying operating loads for the blade and corresponding shifts in working conditions. In contrast, the test rig assembles the working components into specific attitudes and applies loads to the blade using actuators. The geometric relationship of the mechanism can be obtained through the triangle $\triangle ABC$:

$$S \times \cos\alpha_1 + a \times \cos\alpha_3 = b, \tag{1}$$

$$S^2 = a^2 + b^2 - 2ab\cos\alpha_3, \tag{2}$$

where α_1 represents the angle between AB and BC, α_2 is the angle between BC and the vertical direction, and α_3 denotes the angle between AC and BC. The variables a and b correspond to the distances between joint points AC and BC, respectively. S is the length between Points A and B, calculated by the cylinder stroke. The relationship between the component attitudes and cylinder strokes is established through Equations (3)–(5), leveraging the easily measurable cylinder strokes in data acquisition experiments. Here, the values of a and b are constants. L_B and L_H denote the longitudinal and vertical projections of the distance between BC points, respectively. Given that the angle between the lift cylinder and the vertical direction on the virtual VTR consistently measures 27°, the influence of the angle should be considered in the calculation. Equation (6) below is utilized to convert the lift-cylinder oil pressure into a target signal suitable for the virtual VTR. In this equation, F_A represents the cylinder driving force converted from the measured oil pressure and the size of the cylinder cavity and F_T is the transformed lift-cylinder target signal.

$$\alpha_1 = \arccos\left(\frac{b - a \times \cos\left[\arccos\left(\frac{a^2 + b^2 - S^2}{2ab}\right)\right]}{S}\right), \tag{3}$$

$$\alpha_2 = \arctan\left(\frac{L_B}{H_B}\right), \tag{4}$$

$$\beta = \alpha_2 - \alpha_1, \tag{5}$$

$$F_T = F_A \frac{\cos\beta}{\cos 27°}. \tag{6}$$

3.2 | Original signal processing

Given the symmetrical distribution of the eight spherical joints connecting each arm at the back of the blade, this analysis focuses solely on the force information pertaining to the left half.

Figure 11 illustrates the target signal, comprising joint forces for each arm derived from surface strains, material properties, and cross-sectional areas, as well as the lift-cylinder driving force computed based on the attitude relationship and oil pressure. Owing to the rapid response of the control valves, the lift-cylinder joint force shows sporadic spikes at moments when the valves switch positions. Since the entire model was initially in a suspended position, the bulldozer descends to the ground under the influence of gravity after the simulation begins. As a result, the initial load experiences considerable instability and fluctuations, phenomena that would not manifest in an actual working environment and can be safely disregarded. Observing the data, significant variations in loads are evident at different working stages, highlighting the segmented nature
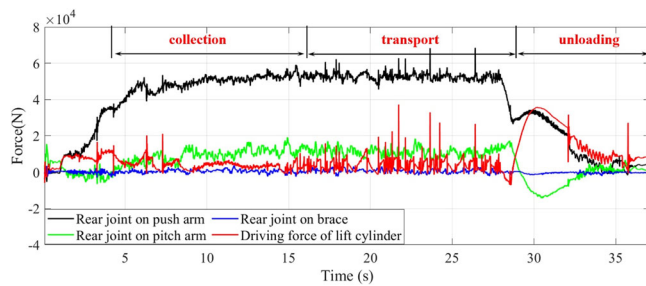

FIGURE 11 Virtual VTR target signals converted from experimental data.

of the operations. Given the bulldozer's cyclic nature, with soil collection and transport as the primary tasks, this paper focuses on extracting data from these two stages as target signals.

3.3 | Virtual VTR

The virtual VTR comprises the working components, actuators, and sensors. The actuator plays a pivotal role in implementing active vibration control, applying function expressions to the joint entities or force entities of the component to correlate input signals in different directions. The correct application of the boundary condition to the working components is crucial for the effectiveness of the analysis results. It should align with the loading mode and constraint conditions of the virtual VTR provided by the project team, as depicted in Figure 12. The reference frame is defined as follows: the X-axis is directed laterally, the Y-axis is directed vertically, and the Z-axis is directed longitudinally. The bulldozer blade primarily experiences lateral force in the X-direction, vertical force in the Y-direction, and longitudinal force in the Z-direction. To facilitate research and fatigue test loading, the component forces in each direction are concentrated in the middle position of the virtual actuators. Forces and constraints are applied at the main node, simplifying the load on the blade into six single-direction axial forces. The effect of the moment is treated as equivalent to two same-direction forces. Six excitation loads in the X, Y, and Z directions equate to torques around the Y, Z, and X axes, respectively. Theoretically, iteration effectiveness is independent of the condition type and depends on the system's degrees of freedom. Currently, six degrees of freedom are assigned, ensuring convergence without any omissions. This approach enables the simulation of the force and torque of the dozer blade. The virtual VTR is constrained at the chassis behind the lift cylinders and
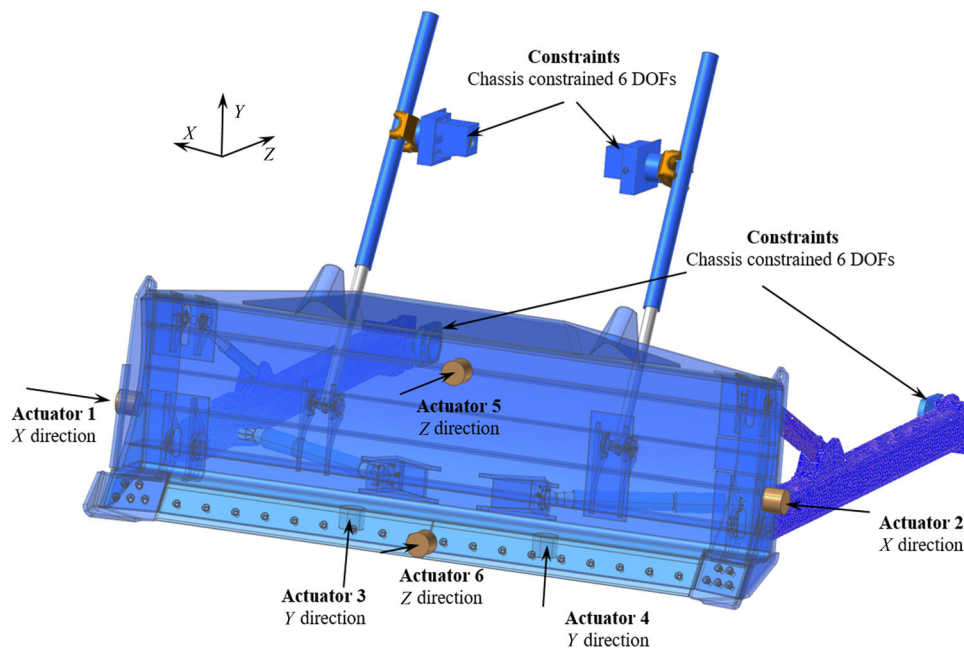

FIGURE 12 Constraints and excitation actuators of a virtual VTR.

Sensor 7
Axial force of left lift cylinder.

Sensor 1
Z-directional force of rear spherical joint on push arm.

Sensor 3
Z-directional force of rear revolute joint on pitch arm

Sensor 5
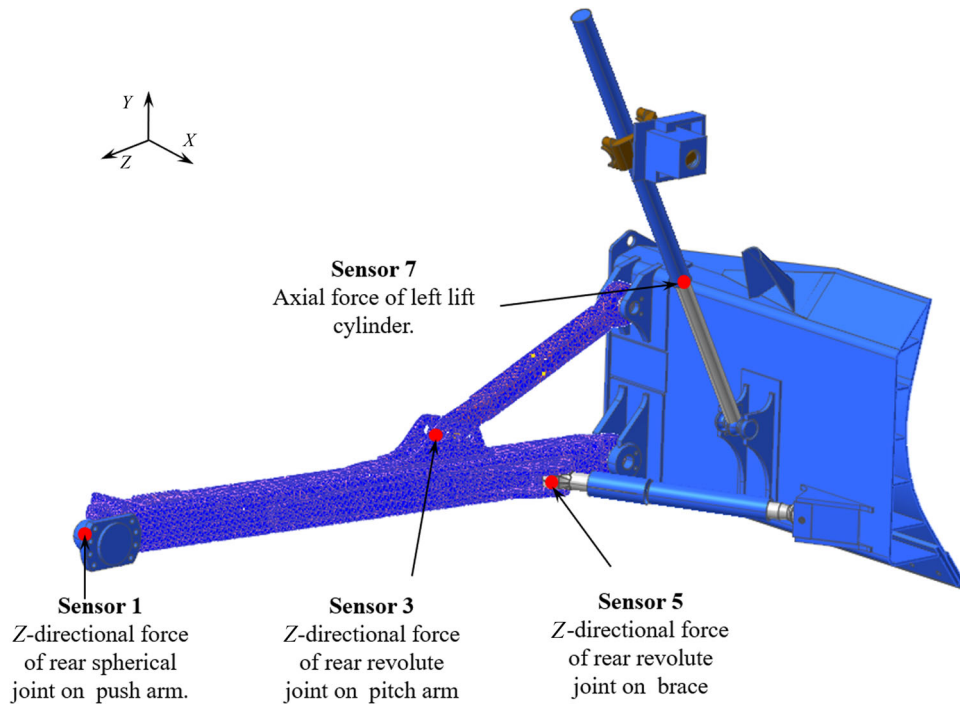Z-directional force of rear revolute joint on brace

FIGURE 13 Sensors location of a virtual VTR.

push arms. Sensors are used to acquire the iterative response signal, which is then compared with the target signal. The position of the virtual sensor aligns with the collected response signal position. Too many sensors will lead to calculation redundancy, and too few sensors will lead to inaccurate load transfer on some paths. Therefore, it is necessary to analyze the load transfer path and set the sensor position according to the load distribution at the joint. The rear spherical joints on push arms, the rear revolute joints on the pitch arm, the rear revolute joints on the brace, and the oil inlet on the lift cylinder are selected as installation positions, as shown in Figure 13.

4 | VIRTUAL ITERATION TECHNOLOGY

4.1 | Principle

Essentially, the result of the response of a structural system is known to solve for the input signal that causes that response. Typically, the structural system is a nonlinear system with each parameter known. The virtual iterative technique for solving loads constitutes an inverse problem aimed at resolving nonlinear equations. This process encompasses two integral components: system identification and deviation correction. System identification involves computing the FRF of the system. The FRF is derived from a transfer function that encapsulates system characteristics, obtained through a signal processing course that transforms time signals into frequency signals. Given the inherent nonlinearity of the entire test rig and the fact that the measurement of the system's FRF matrix is rooted in a linear system, the inverse FRF necessitates correction using a deviation

correction algorithm. The specific procedural steps of the virtual iteration technique are depicted in Figure 14.

To explain the characteristics of the virtual VTR, a white noise signal $A^0(s)$ is initially introduced, leading to the generation of a response signal $S^0(s)$. Subsequently, the FRF $F(s)$ is calculated using Equation (7).

$$F(s) = S^0(s)/A^0(s). \tag{7}$$

Subsequently, the inverse function of the FRF $F^{-1}(s)$ is determined using the pseudo-inverse method. The time-domain target signal $T(t)$ is then transformed into the frequency-domain target signal $T(s)$ through the application of fast Fourier transform (FFT):

$$T(s) = \text{FFT}[T(t)]. \tag{8}$$

The initial input signal $A^1(s)$ is obtained through the inverse transfer function $F^{-1}(s)$ and the measured target signal $T(s)$, as shown in Equation (9).

$$\begin{bmatrix} A^1_1 \\ A^1_2 \\ \dots \\ A^1_6 \end{bmatrix} = \begin{bmatrix} F_{11} & F_{12} & \dots & F_{18} \\ F_{21} & F_{22} & \dots & F_{28} \\ \dots & \dots & \dots & \dots \\ F_{61} & F_{62} & \dots & F_{68} \end{bmatrix}^{-1} \begin{bmatrix} T_1 \\ T_2 \\ \dots \\ T_8 \end{bmatrix}. \tag{9}$$

The initial frequency-domain input signal $A^1(s)$ undergoes Fourier inverse transform to yield the initial time-domain input signal $A^1(t)$. Subsequently, the obtained time-domain input signal $A^1(t)$ is applied to the corresponding actuator within the virtual VTR. The resultant first time-domain response signal $S^1(t)$ is acquired
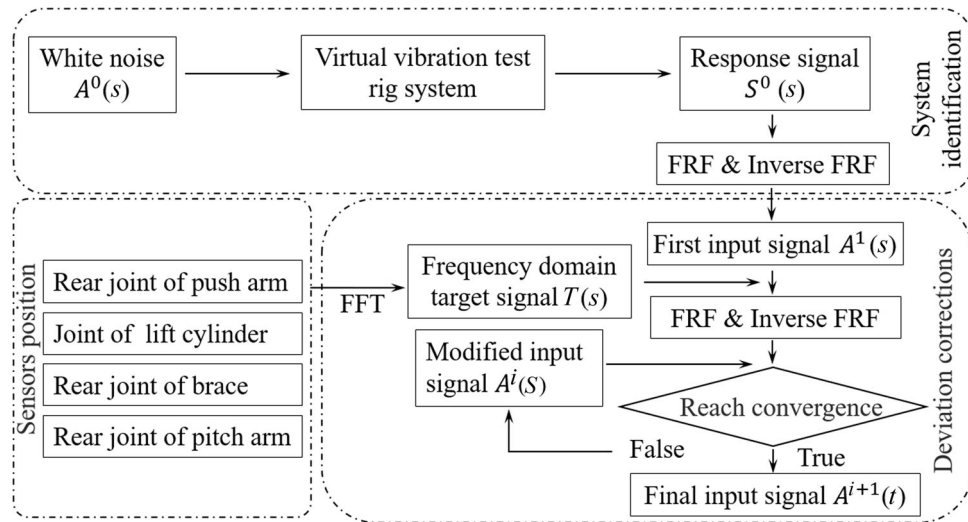
FIGURE 14 Virtual iteration technique flow.

through the virtual sensor. The collected response signal from the virtual sensor in the corresponding iterative sequence is then compared with the target signal obtained from experimental measurements. The error $E^1(t)$ between the time-domain target signal $T(t)$ and the time-domain response signal $S^1(t)$ is calculated using the following equation:

$$E^1(t) = T(t) - S^1(t). \qquad (10)$$

$E^1(t)$ undergoes Fourier transformation to derive the frequency-domain response error $E^1(s)$. This error signal in the frequency domain is then adjusted by multiplying it with the iterative gain coefficient β. Subsequently, the next input signal, $A^2(s)$, is computed. Maintaining the inverse FRF and continually modifying the gain coefficient during the iterative process, multiple iterations are conducted until the simulation result aligns with the measured target signal, reaching a convergent state. The final time-domain input signal, $A^{i+1}(t)$, applied to the virtual actuator, is determined through the correction algorithm, as shown in the following equation:

$$A^{i+1}(s) = A^i(s) + \beta E^i(s) \times F^{-1}(s). \qquad (11)$$

Figure 15 displays the time-domain input signals for six actuators under straight bulldozing conditions. The input signal derived from the final iteration is subsequently reintroduced into the rigid–flexible coupling MBD model using the AKISPI function[34] for fatigue analysis.

4.2 | Data verification

After completing the iteration, the results require examination to determine whether the response signal obtained aligns with the target signal measured in the test. The primary comparison is drawn from the time domain and the change trend of the root mean square
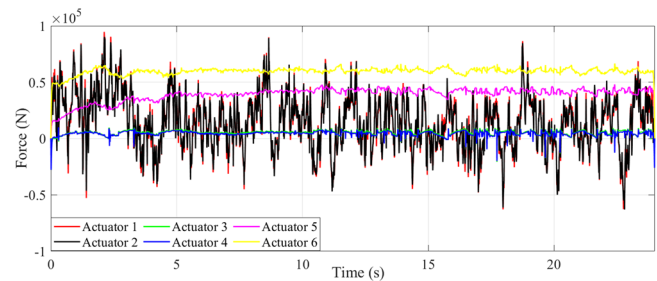

FIGURE 15 Input signals of the actuator under straight bulldozing conditions.
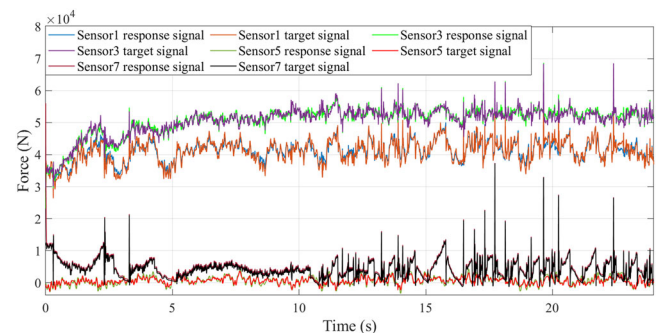

FIGURE 16 Comparison of the target signal and the response signal under straight bulldozing conditions.

(RMS) error, aiming to achieve high accuracy in the input signal. Figure 16 depicts the time-domain comparison results between the final iterative response signal collected by the sensor and the experimental target signal under straight bulldozing conditions. The results indicate a slight deviation primarily caused by uneven material changes in front of the blade during the soil collection phase, leading to slight oscillations. However, the overall amplitude and change

trend remain consistent. The RMS error is utilized to quantify the reproduction quality and is defined as

$$\text{RMS} = \sqrt{\frac{\sum_{i=1}^{N}[T(i) - S(i)]^2}{\sum_{i=1}^{N}[T(i)]^2}} \times 100\%, \qquad (12)$$

where N represents the total number of signal sampling points; $T(i)$ and $S(i)$ denote the target and response signals, respectively. It is essential to highlight that the RMS error of the last iteration is 0.06 under straight bulldozing conditions, as depicted in Figure 17. This demonstrates the effective reproduction of the input signal by the proposed method in the virtual VTR. It is noteworthy that the first 10 iterations showed a marked improvement, while subsequent iterations had a limited impact.

5 | FATIGUE ANALYSIS

The fatigue analysis of the push arm involves addressing low-stress, long-life issues, specifically high-cycle fatigue. To tackle this, we used a stress-based multi-axial fatigue analysis method.[35,36] Control parameters included the stress concentration coefficient and stress-time history at critical locations prone to structural fatigue. Utilizing the rain-flow counting method, we determined the stress amplitude, the mean stress value, and the cycle count for each stress amplitude. Subsequently, fatigue damage assessment and life prediction analyses for structural components were conducted, using S–N curves and the linear cumulative damage theory.[37]

5.1 | Fatigue theory

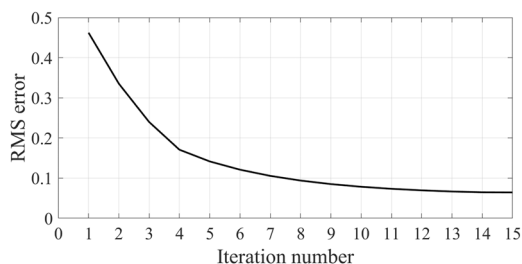The bulldozer's push arm is constructed from a square steel pipe welded together with supporting plates. The push arms are composed of HF50_10 steel, a material defined in accordance with the SAE J1099 standard.[38] The material parameters are presented in Table 2.

The fatigue analysis of the structure should be grounded in the S–N curve, defining the relationship between stress levels and the number of load cycles leading to material fatigue failure at those stress levels. The S–N curve is constructed based on the Masson–Coffin life criteria, as shown by the following equation:

$$\frac{\Delta\sigma}{2} = \sigma_f'(2N_f)^b, \qquad (13)$$

where $\Delta\sigma/2$ is the normal stress amplitude for a cycle, σ_f' is the fatigue strength coefficient, $2N_f$ is the reversals to failure, and b is the fatigue strength exponent.

Generally, the S–N curve for a material is determined under symmetric cyclic loading, indicating conditions of average stress. However, the push arm typically experiences random amplitude varying loads with a nonzero average value of load cycles.[39,40] To account for this, the Goodman algorithm is used to adjust the stress–life curve, equating asymmetric stress cycles to symmetric stress cycles, as presented in the following equation:

$$\frac{\sigma_\alpha}{S_e} + \frac{\sigma_m}{S_u} = 1, \qquad (14)$$

where σ_α is the stress amplitude, S_e is the effective alternating stress at failure for a lifetime, S_u is the ultimate strength, and σ_m is the mean normal stress for a cycle.

The modification involved assigning values to fatigue-influencing factors, including the notch factor amp (1.2), the surface factor (0.9), and other factors (1). Figure 18 depicts the stress–life curves for the push arm, directly retrieved from the RecurDyn software material library. The S–N curves show two variations: the blue curve disregards the impact of fatigue-influencing factors, while the black curve incorporates these factors into the analysis.
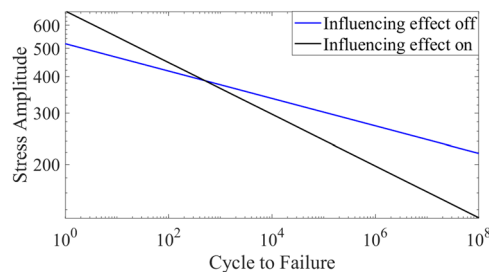

FIGURE 17 Variation curve of the RMS error under straight bulldozing conditions.

FIGURE 18 Stress–life curves for the push arms.

TABLE 2 Parameters of HF50_10 steel.

Yield stress (MPa)	Ultimate stress (MPa)	Fatigue strength coefficient	Fatigue strength exponent	Fatigue ductility coefficient	Fatigue ductility exponent	Cyclic strength coefficient	Cyclic strength hardening exponent
359	490	536	−0.047	4.118	−0.883	481	0.049

5.2 | Stress–time histories and rain flow counting

Crack initiation and propagation primarily occur on the structure's surface. Therefore, it is necessary to use tensor transformation to convert the structural stress obtained from finite element analysis into the stress on the surface of the elements. Based on the theoretical analysis of the bulldozer's working component strength and the finite element analysis of the push arm, the stress contours of the push arms under the maximum stress state are presented in Figure 19. It can be observed that the maximum stress occurs at 1100 mm from the rear joint of the push arm. A comparison of the stress–time variation at the surface nodes with the most severe damage is shown in Figure 20. In the co-simulation, the material model is represented as a discrete particle group with adhesion. However, the particle size distribution differs from the actual scenario, lacking the genuine interlocking effect. While the damping coefficient has been adjusted, the model still shows noise, and the stress amplitude range is marginally larger than the results obtained through iteration. The maximum stress at the monitoring point is 34 MPa by co-simulation under straight bulldozing conditions. The result by VTR is 28 MPa. However, these maximum stresses are well below the yield stress of the push arms, indicating that the push arm meets the requirements.

Life prediction based on the S–N curve necessitates cyclic external loads. Therefore, the rain-flow counting method is used to convert random loads into cyclic loads with variable amplitudes.[41,42] Figure 21 displays the cycle graph obtained after rain-flow counting for the stress–time history. The results indicate that the stress amplitude, the stress mean value, and the number of cycles for each stress amplitude generated by the iteration are smaller, but the overall coincidence degree is high.

5.3 | Fatigue life calculation

The fatigue damage accumulation theory serves as the critical foundation for life prediction. Failures in engineering mechanical arms are predominantly attributed to the accumulation of fatigue damage in the weld seams and structural stress concentrations under variable amplitude loads. Consequently, the cumulative damage theory of linear fatigue, specifically the Palmgren–Miner cumulative damage criterion, is used to calculate high-cycle fatigue life. Widely utilized in engineering practice for accurate fatigue life calculations, this method operates on the assumption that damages resulting from various stress levels are independent and can be linearly superimposed.[43] Fatigue damage occurs when the cumulative damage reaches a specified value. The total fatigue life is computed based on fatigue life and the number of cycles using the following equation:

$$D = \sum_{i=1}^{n} \frac{n_i}{N_i}, \ \lambda = \frac{1}{D}, \tag{15}$$

where N_i is the fatigue life corresponding to the ith stress σ_i of the push arms, n_i is the number of cycles corresponding to the ith stress σ_i, n represents the total number of stresses, D is the total damage, and λ is the total fatigue life of the push arms.

Figure 22 depicts life contours and damage distributions of the push arms under the straight bulldozing conditions. Parts with the shortest service lives are highlighted in red, while those with the
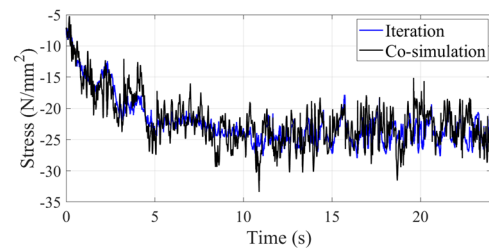

FIGURE 20 Stress–time histories of push arms under straight bulldozing conditions.
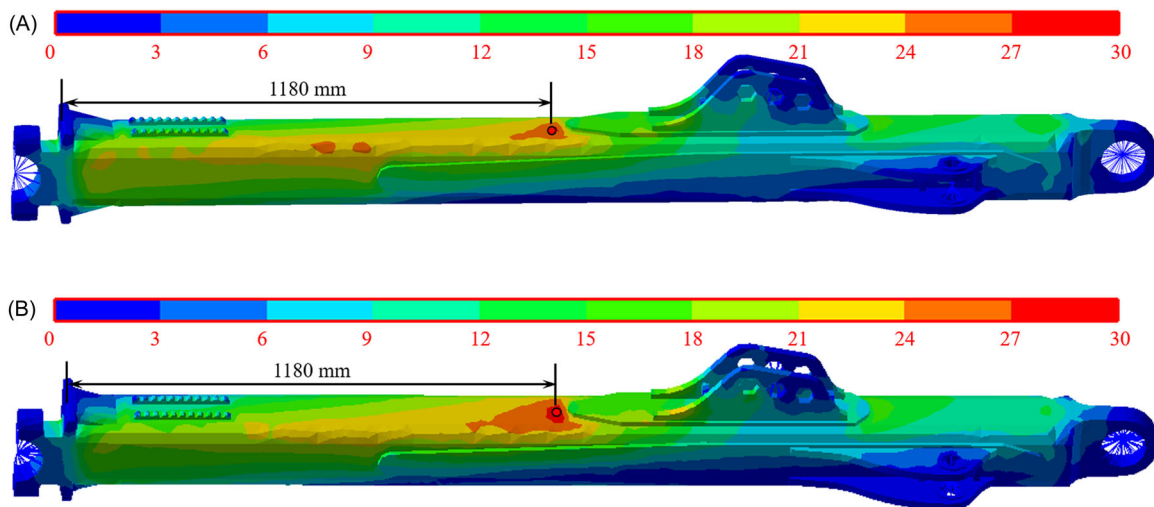

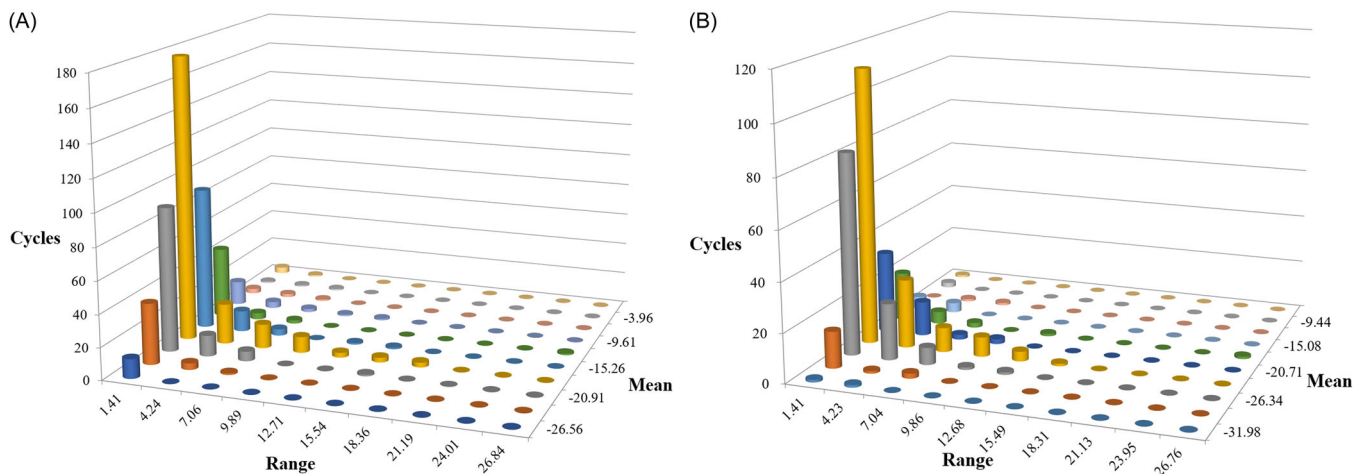**FIGURE 19** Stress contours under straight bulldozing conditions: (A) co-simulation and (B) iteration.

FIGURE 21 Rain-flow counting results under straight bulldozing conditions: (A) co-simulation and (B) iteration.
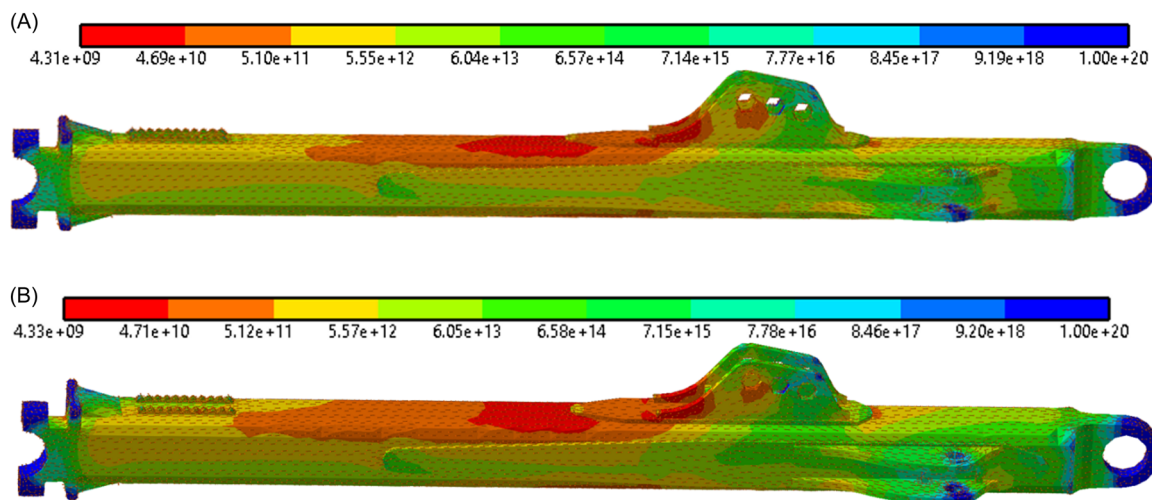

FIGURE 22 Life contour and damage distribution under straight bulldozing conditions: (A) co-simulation and (B) iteration.

longest service lives are marked in blue. It is evident that the rear section of the supporting plates connected to the pitch arm is more prone to developing cracks under straight bulldozing conditions. The minimum cycle life obtained is relatively large due to considering only relatively stable data from the soil collection and transportation stages. Analysis and comparison of the two structural fatigue life prediction methods reveal consistent calculated damage distribution of the push arm. This confirms the reliability of fatigue analyses based on the virtual VTR. Table 3 outlines the simulation time calculated by the two methods, clearly demonstrating the efficiency advantage of virtual iteration.

TABLE 3 The stress concentration region and the maximum stress.

Condition	Straight bulldozing conditions
Minimum life region	The rear part of the supporting plates connected with the pitch arm
Minimum cycle life (co-simulation)	4.31×10^9
Minimum cycle life (iteration)	4.33×10^9
Simulation time (co-simulation)	720 min
Simulation time (iteration)	20 min

6 | CONCLUSIONS

According to the differences of component attitudes in the working condition and the VTR condition, this paper establishes the relationship between the load distribution and the kinematic relationship

of a dozer's working components in theory. Meanwhile, one virtual VTR is established to analyze the fatigue life of push arms, which is also verified by the fatigue life analyzed by using the load–time history. The specific contributions are as follows:

1. With respect to the reference frame of blade, the transformation formulation is provided to reflect the attitude relationship of the working components in straight bulldozing conditions and on the VTR.

2. The relationship between the component attitudes and cylinder strokes is also established, because the cylinder strokes are easy to measure in the data acquisition experiments.

3. One virtual VTR is established to analyze the fatigue life of the dozer push arms, and the analysis results match well with the fatigue life given by load–time history of co-simulation; the modeling process is illustrated in detail for reference.

4. Not only the simulation results but also the real working load spectrum can be used as the target signals of the virtual VTR to generate the input signals; the virtual VTR is an efficient and economic tool for the fatigue analysis.

5. The research also guides the data acquisition experiment—the cylinder strokes of the construction machinery should also be measured to accurately determine the load distribution with respect to the working attitudes of the components.

Due to the limitations of the experimental conditions, only co-simulation results of the virtual physical field are used to verify the iterative model. The verification with the physical VTR will be conducted in the future. In addition, because of the challenges in load decomposition under special working conditions and the complexity of constructing control logic and hydraulic schematic diagrams in combined working conditions, load data for conditions such as tilt bulldozing and turning will be iterated.

ACKNOWLEDGMENTS

CONFLICT OF INTEREST STATEMENT

The authors declare no conflict of interest.

DATA AVAILABILITY STATEMENT

The data that support the findings of this study are available from the corresponding author upon reasonable request.

ORCID

Lei Hou https://orcid.org/0009-0006-4381-3775

REFERENCES

1. Liu G, Luo G, Zhang Z, Yang X, Wu D. Fatigue life analysis and structure performance improvement of bulldozer working device based on ANSYS. Paper presented at: 3rd IEEE Information Technology and Mechatronics Engineering Conference (ITOEC), Chongqing, China, 3-5 October 2017. 2017.

2. Qin C, Ma C, Li L, Sun X, Liu Z, Sun Z. Development and application of an intelligent robot for rock mass structure detection: a case study of Letuan tunnel in Shandong, China. *Int J Rock Mech Min Sci*. 2023;169:105419.

3. Kogan J. On the durability analysis of machinery components. *Int J Fatigue*. 1981;3:27-30.

4. Beretta S, Clerici P. A novel test rig for narrow band random fatigue under rotating bending. *Int J Fatigue*. 1997;19:457-460.

5. Gao N, Brown M, Miller K, Reed P. An effective method to investigate short crack growth behaviour by reverse bending testing. *Int J Fatigue*. 2007;29:565-574.

6. Koch U, Wiedemann D, Ulbrich H. Model-based MIMO state-space control of a car vibration test rig with four electromagnetic actuators for the tracking of road measurements. *IEEE Trans Ind Electron*. 2011;58:5319-5323.

7. Lorenz SJ, Sadeghi F, Trivedi HK, Kirsch MS. Investigation into rolling contact fatigue performance of aerospace bearing steels. *Int J Fatigue*. 2023;172:107646.

8. Wang PH, Xiang QY, Królczyk G, Lu PM, Wang BH, Li ZX. Dynamic modeling of a hydraulic excavator stick by introducing multi-case synthesized load spectrum for bench fatigue test. *Machines*. 2022; 10(9):741.

9. Yin Y, Grondin GY, Obaia KH, Elwi AE. Fatigue life prediction of heavy mining equipment. Part 1: fatigue load assessment and crack growth rate tests. *J Constr Steel Res*. 2007;63:1494-1505.

10. Bae H-R, Ando H, Nam S, Kim S, Ha C. Fatigue design load identification using engineering data analytics. *J Mech Des*. 2015;137:011001.

11. Dressler K, Speckert M, Bitsch G. Virtual durability test rigs for automotive engineering. *Veh Syst Dyn*. 2009;47:387-401.

12. Oppermann H, Bäcker M, Langthaler T. Computing drive signals at a virtual test rig: another step towards CAE-based durability analysis. Paper presented at: Meeting on Numerical Analysis and Simulation in Vehicle Engineering, Wurzburg, Germany, 1-2 October 2002. 2002.

13. Kim HS, Yim HJ. Computational durability prediction of body structures in prototype vehicles. *Int J Automot Technol*. 2002;3:129-135.

14. Sendur P, Ozcan U, Ozoguz B. A methodology to design multi-axis test rigs for vibration and durability testing using frequency response functions. *Proc Meet Acoust*. 2017;30:065001.

15. Li D, Tian J, Shi S, Wang S, Deng J, He S. Lightweight design of commercial vehicle cab based on fatigue durability. *Comput Model Eng Sci*. 2023;136:421-445.

16. Wang T, Wang L, Wang Y. Assessment of the locations of fatigue failure in a commercial vehicle cab using the virtual iteration method. *Proc Inst Mech Eng D J Automob Eng*. 2017;231:84-98.

17. Bian X, Ma S, Yang J, Ge X. Fatigue analysis of truck cab based on virtual iteration method. *Mach Des Res*. 2017;33:170-173.

18. Ge W, Gong C, Liu Z, Duan L, Huang H. Load extraction of leaf-spring bushing based on road load data and test-rig fatigue test. *J Mech Strength*. 2020;42:43-49.

19. Daley S, Owens DH, Hatonen J. Application of optimal iterative learning control to the dynamic testing of mechanical structures. *Proc Inst Mech Eng I J Syst Control Eng*. 2007;221:211-222.

20. Wang X, Cong D, Yang Z, Xu S, Han J. Modified quasi-Newton optimization algorithm-based iterative learning control for Multi-Axial road durability test rig. *IEEE Access*. 2019;7:31286-31296.

21. Mueller T, Endisch C. Compensation techniques for iterative rig control in multi-axial durability testing. Paper presented at: 21st IEEE International Conference on Emerging Technologies and Factory Automation (ETFA), Berlin, Germany, 6-9 September 2016. 2016.

22. Wan Y, Song X, Yu L, Yuan Z. Load identification model and measurement method of loader working device. *J Vib Meas Diagn*. 2019; 39:582-589.

23. Kim S-H, Lee Y-S, Sun D-I, et al. Development of bulldozer sensor system for estimating the position of blade cutting edge. *Automat Constr*. 2019;106:102890.

24. Czerlunczakiewicz E, Majerczak M, Bonato M. Variability of fatigue simulation predictions for automotive components. Paper presented at: 69th Annual Reliability and Maintainability Symposium (RAMS), Orlando, FL, USA, 23-26 January 2023. 2023.

25. Liu JY, Hong JZ. Geometric stiffening effect on rigid-flexible coupling dynamics of an elastic beam. *J Sound Vib*. 2004;278:1147-1162.

26. Heirman GHK, Desmet W. Interface reduction of flexible bodies for efficient modeling of body flexibility in multibody dynamics. *Multibody Syst Dyn*. 2010;24:219-234.

27. Zhu X, Pan L, Sun Z, Wan Y, Huang Y, Choi J-H. Simulation tool for dozer data acquisition. *Automat Constr*. 2022;142:104522.

28. Pan L, Zhu X, Li Y, Guan T. Lightweight design of an electric tricycle frame considering dynamic stress in driving conditions. *Int J Automot Technol*. 2021;22:1075-1085.

29. Shin YJ, Jeong JS, Jun CW, Sohn JH. Interacting analysis between wheel and sand particles based on DEM and its validation with experiments. *J Mech Sci Technol*. 2020;34:4537-4544.

30. Wasfy T, Jayakumar P. Next-generation NATO reference mobility model complex terramechanics-part 1: definition and literature review. *J Terramech*. 2021;96:45-57.

31. Awuah E, Zhou J, Liang Z, et al. Parametric analysis and numerical optimisation of Jerusalem artichoke vibrating digging shovel using discrete element method. *Soil Tillage Res*. 2022;219:105344.

32. Tekeste MZ, Way TR, Syed Z, Schafer RL. Modeling soil-bulldozer blade interaction using the discrete element method (DEM). *J Terramech*. 2020;88:41-52.

33. Richter C, Roessler T, Otto H, Katterfeld A. Coupled discrete element and multibody simulation, part I: implementation, verification and validation. *Powder Technol*. 2021;379:494-504.

34. Yan L, Cui G-H, Yuan H-Z, Zhou H-D. The kinematic solving of the 4-RPC redundantly actuated parallel mechanism based on RecurDyn. *Modul Mach Tool Autom Manuf Tech*. 2013:36-39.

35. Delahay T, Palin-Luc T. Estimation of the fatigue strength distribution in high-cycle multiaxial fatigue taking into account the stress-strain gradient effect. *Int J Fatigue*. 2006;28:474-484.

36. Baumgartner J, Waterkotte R, Hesseler J. Fatigue assessment of a welded automotive differential under multiaxial and variable amplitude loading. *Int J Fatigue*. 2021;149:106292.

37. Zhang L, Jiang B, Zhang P, et al. Methods for fatigue-life estimation: a review of the current status and future trends. *Nanotechnol Precis Eng*. 2023;6:025001.

38. Engineers, S.o.A. SAE J1099. Rev. 2002. Available online: https://www.docin.com/p-1750860016.html

39. Li WB, Xu YR, Hu N, Deng MX. Impact damage detection in composites using a guided wave mixing technique. *Meas Sci Technol*. 2020;31:014001.

40. Jiang C, Li W, Deng M, Ng C-T. Quasistatic pulse generation of ultrasonic guided waves propagation in composites. *J Sound Vib*. 2022;524:116764.

41. Glinka G, Kam J. Rainflow counting algorithm for very long stress histories. *Int J Fatigue*. 1987;9:223-228.

42. Meggiolaro MA, de Castro JTP. An improved multiaxial rainflow algorithm for non-proportional stress or strain histories—part II: the modified Wang-Brown method. *Int J Fatigue*. 2012;42:194-206.

43. Zhao H, Wang G, Wang H, Bi Q, Li X. Fatigue life analysis of crawler chain link of excavator. *Eng Fail Anal*. 2017;79:737-748.

AUTHOR BIOGRAPHIES

Lei Hou is a graduate student of Mechanical Engineering at Shandong University, Jinan, China. His research interests include multibody dynamics and fatigue vibration test rig design.
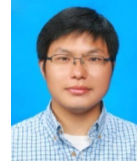
Weibin Li is a professor of Aerospace Engineering at Xiamen University, Xiamen, China. His research interests include nondestructive testing and structural health monitoring of aerospace critical components, and theory and method of nonlinear ultrasonic detection.

Wenyan Gu is a doctoral candidate in Mechanical Engineering at Shandong University, Jinan, China. Her research interests include structure and process integration design.

Zizheng Sun is a researcher of Qilu Transportation at Shandong University, Jinan, China. His research interests include underground engineering disaster prevention and control, tunnel construction, intelligent detection, and data assimilation.

Xiangqian Zhu is a professor of Mechanical Engineering at Shandong University, Jinan, China. His research interests include multibody dynamics and working load identification and development of software for flexible multibody dynamics.

Jin-Hwan Choi is a professor at KyungHee University of Mechanical Engineering, Seoul, South Korea. His research interests include rigid and flexible multibody dynamics, tracked vehicle system dynamics, and data-driven CAE using deep neural network.